AGU PUBLICATIONS

JGR

Journal of Geophysical Research: Atmospheres

RESEARCH ARTICLE
10.1002/2013JD020472

Special Section:
Suomi NPP Calibration and Validation Scientific Results

This article is a companion to *Jaross et al.* [2014] doi:10.1002/2013JD020482.

Key Points:
- The SNPP OMPS nadir sensors are performing nominally
- Solar calibration sequence modified in orbit to minimize diffuser features
- The sensors are stable, with any degradation being correctable

Correspondence to:
C. J. Seftor,
colin.seftor@ssaihq.com

Citation:
Seftor, C. J., G. Jaross, M. Kowitt, M. Haken, J. Li, and L. E. Flynn (2014), Postlaunch performance of the Suomi National Polar-orbiting Partnership Ozone Mapping and Profiler Suite (OMPS) nadir sensors, *J. Geophys. Res. Atmos.*, *119*, doi:10.1002/2013JD020472.

Received 30 JUN 2013
Accepted 12 FEB 2014
Accepted article online 14 FEB 2014

Postlaunch performance of the Suomi National Polar-orbiting Partnership Ozone Mapping and Profiler Suite (OMPS) nadir sensors

C. J. Seftor[1], G. Jaross[2], M. Kowitt[1], M. Haken[1], J. Li[1], and L. E. Flynn[3]

[1]Science Systems and Applications, Inc., Lanham, Maryland, USA, [2]NASA Goddard Space Flight Center, Greenbelt, Maryland, USA, [3]Satellite Applications and Research, NOAA, College Park, Maryland, USA

Abstract The prelaunch specifications for nadir sensors of the Ozone Mapping and Profiler Suite (OMPS) were designed to ensure that measurements from them could be used to retrieve total column ozone and nadir ozone profile information both for operational use and for use in long-term ozone data records. In this paper, we will show results from our extensive analysis of the performance of the nadir mapper (NM) and nadir profiler (NP) sensors during the first year and a half of OMPS nadir operations. In most cases, we determined that both sensors meet or exceed their prelaunch specifications. Normalized radiance (radiance divided by irradiance) measurements have been determined to be well within their 2% specification for both sensors. In the case of stray light, the NM sensor is within its 2% specification for all but the shortest wavelengths, while the NP sensor is within its 2% specification for all but the longest wavelengths. Artifacts that negatively impacted the sensor calibration due to diffuser features were reduced to less than 1% through changes made in the solar calibration sequence. Preliminary analysis of the disagreement between measurements made by the NM and NP sensors in the region where their wavelengths overlap indicates that it is due to shifts in the shared dichroic filter after launch and that it can be corrected. In general, our analysis indicates that both the NM and NP sensors are performing well, that they are stable, and that any deviations from nominal performance can be well characterized and corrected.

1. Introduction

The Ozone Mapping and Profiler Suite (OMPS) on board the Suomi National Polar-orbiting Partnership satellite is a complete sensor algorithm system developed to meet the accuracy and precision specifications for total column ozone and ozone profile retrievals detailed originally in the National Polar-orbiting Operational Environmental Satellite System program and currently in the successor Joint Polar Satellite System (JPSS) program. The NM sensor and its algorithm are designed to meet the top-level specifications for total column ozone retrievals, while the limb profiler (LP) sensor and its algorithm are designed to meet the top-level specifications for ozone profile retrievals. Along with the NM and LP sensors, OMPS contains the NP sensor; while the NP sensor/algorithm system is not designed to satisfy the JPSS total column or ozone profile requirements, its addition to the suite provides retrievals that are an important link to the historical data sets from the Solar Backscatter Ultraviolet (SBUV) and SBUV/2 series of sensors [*DeLand et al.*, 2012], and they provide a direct means to evaluate limb retrievals and link them to the historical record. Measurements from the three sensors therefore provide retrievals for use in multiple roles, including operational (as input to forecasting models, etc.), research (on ozone chemistry, dynamics, etc.), and the continuation of long-term total column ozone and ozone profile records begun in 1978 by the Total Ozone Mapping Spectrometer and the SBUV and SBUV/2 sensors [*Stolarski and Frith*, 2006]. In order to fulfill these roles, the performance of the sensors must be fully characterized, and any performance issues must be well understood. Furthermore, the performance of the sensors must either be stable with time, or any changes they exhibit must be correctable.

This paper describes our analysis of the OMPS nadir sensors during their first year and a half of operation. Since one metric used to evaluate on-orbit sensor performance is to determine whether that performance matches prelaunch specifications, we provide the specifications for each nadir sensor in section 1. We also provide a brief description of both nadir sensors in this section; for a complete description, see the paper of *Dittman et al.* [2002]. In section 2, we present results showing the performance of the sensors and how they

Table 1. Sensor Specifications for OMPS Nadir Sensors

Parameter	Value
Both	
Radiance–RMS uncertainty	8%
Irradiance–RMS uncertainty	7%
Radiance/irradiance ratio–RMS uncertainty	
Absolute	2%
Relative (between wavelengths)	0.5%
Wavelength calibration–RMS uncertainty	0.015 nm
On-orbit wavelength shift sensitivity	0.01 nm
Stray light (before correction)	2%
Nonlinearity knowledge (zero input signal to full CCD well)	0.2%
Pixel-to-pixel response knowledge	0.2%
Nadir Mapper	
Wavelength range	300–380 nm
Minimum SNR (all wavelengths)	1000
Nadir Profiler	
Wavelength range	250–310 nm
Minimum SNR	
252 nm	35
273 nm	100
283 nm	200
287 nm	250
292 nm	400
297 nm	400
302 nm	400
306 nm	400

compare to their specifications, and we point out issues with each sensor and areas needing further examination and evaluation. In section 3, we discuss their calibration and initial results concerning their long-term stability. In section 4, we provide a brief summary.

Although analysis of the LP sensor is detailed in a companion paper [*Jaross et al*., this issue], many aspects of its performance are similar to the performance of the nadir sensors; since the analysis of these aspects results in similar conclusions, they are therefore covered here. Measurements from the NM and NP sensors are provided, via the Sensor Data Record (SDR) algorithm, to the respective total column and ozone profile retrieval algorithms for the creation of the NM total column Environmental Data Record (EDR) and NP ozone profile intermediate product (IP). The paper of *Wu et al*. [this issue] describes the performance of the SDR algorithm, while an on-orbit evaluation of the total column ozone and ozone profile retrievals from the nadir sensors is provided by another companion paper [*Flynn et al*., this issue].

1.1. Specifications for the OMPS Nadir Sensors

The JPSS top-level requirements for total column ozone retrievals are given in the paper of *Flynn et al*. [this issue]. A set of specifications were derived for the NM sensor from these requirements; these specifications, shown in Table 1, were based on experience with heritage sensors and how different aspects of sensor performance affect the accuracy and precision of the algorithmic retrieval [*Seftor et al*., 2003]. To verify that retrievals from a sensor that conformed to these specifications met the top-level requirements, ozone retrievals were performed using simulated radiances based on radiative transfer models [*Seftor et al*., 2003].

As stated earlier, the NP sensor was not designed to satisfy any JPSS top-level requirements. However, because of its role in providing continuity with nadir ozone profile retrievals from the SBUV/SBUV 2 series of sensors, a set of top-level requirements, shown in the paper of *Flynn et al*. [this issue], was created to specify that the nadir ozone profile retrieval performance was to be similar to heritage performance; as a result, the specifications derived for the NP sensor were similar to the SBUV/2 sensors. These specifications are also shown in Table 1.

1.2. The OMPS Nadir Sensors

The OMPS nadir instrument is composed of two spectrometers that share the same telescope. A dichroic filter downstream of the telescope redirects photons into either the NM or the NP spectrometer. The telescope itself has a 110° total across-track field of view (FOV), resulting in 2800 km instantaneous coverage at the Earth's surface; this is sufficient to provide daily full global coverage at the equator. The telescope includes a pseudo depolarizer [*McClain et al*., 1992] designed to minimize the system's sensitivity to incoming polarization. The dichroic filter is optimized to reflect most of the 250–310 nm light to the NP spectrometer and transmit most of the 300–380 nm light to the NM spectrometer. The two spectrometers' bands overlap from 300 to 310 nm, which is the region where the dichroic filter transitions from reflection to transmission. The spectrometer entrance

slits are located immediately after the split. The NP slit restricts the across-track FOV to the center 16° provided by the telescope.

Once split, the light from each spectrometer is dispersed via a diffraction grating onto one dimension of a two-dimensional charge-coupled device (CCD) located at each spectrometer's focal plane. The second dimension reflects the cross-track spatial coverage provided by the slit aperture and optics. Both CCDs consist of 340 pixels along the spectral dimension and 740 pixels in the across-track spatial dimension. Since the spectra produced by both sensors' dispersive elements are essentially linear as a function of wavelength, curvature and nonlinearity in the image of the slit on the CCD are due primarily to the focusing optics of each sensor. The NM sensor has very little spectral distortion (also known as spectral smile)—less than 1 pixel's width over the full spatial extent of the detector. The spatial distortion, also known as keystone, causes the length of the FOV in the along-track direction to change by 0.2% from the shortest to the longest wavelength. The NP sensor has somewhat more spatial variation, but spectra for a given spatial index are almost as well behaved as those of the NM sensor, which can be fitted by a cubic polynomial as a function of spectral index. The readout from the NM CCD is split, with half the CCD being read out in one spatial direction and half being read out in the other. Due to telemetry bandwidth constraints, the CCD pixel signals are combined in time and across track within the instrument electronics prior to transmission; the effect is a reduction in spatial resolution for both sensors.

For the NM sensor, measurements meeting the 300–380 nm wavelength range specification shown in Table 1 are obtained by illuminating 196 of the 340 pixels in the spectral dimension. In the across-track dimension, 708 pixels are illuminated. For nominal operations, the pixel signals are summed into 35 separate "macropixel" FOVs; all but the two outer FOVs contain 20 pixels per macropixel; the left outermost macropixel contains 26 pixels, while the right outermost contains 22. These macropixels were designed to meet the detector noise and spatial cell size requirements listed in Table 1. Gain and nonlinearity corrections are applied to each pixel by the flight electronics prior to summation to compensate for large radiance or sensitivity variations across the macropixel and over the full 7.5 s exposure time. Since the readout of the CCD is split in the center, measurements comprising the central FOV are actually split (although not symmetrically). Rather than rebinning these measurements in ground processing, they can remain split, resulting in 36 cross-track FOVs. In this case, the central two FOVs comprise 12 pixels (30 × 50 km) and 8 pixels (20 × 50 km), respectively.

Because macropixels are constructed in programmable flight electronics, the OMPS nadir temporal (along-track) and spatial (across-track) resolutions are highly configurable. High-resolution measurements, approximately 10 km × 10 km at nadir, have been routinely collected 1 day per week for the first 2 years of the mission. To remain within the telemetry bandwidth constraints, a set of only 59 wavelengths was selected; this selection still allows retrievals of total column ozone and other quantities (such as SO_2) using the current algorithms, albeit with lower SNR values.

For the NP sensor, 147 of the 340 spectral pixels are illuminated, resulting in the 250–310 nm range specified in Table 1. The NP entrance slit illuminates only 93 of the available spatial pixels. All of the pixels are on the same side of the CCD, and they are subsequently combined into a single macropixel. The 147 × 93 pixels are exposed for 38 s, which yields a 250 km × 250 km nadir-looking FOV that is somewhat larger than the SBUV/2 FOV. As with the NM sensor, the NP sensor can be configured to provide higher-resolution measurements by changing the along-track timing and across-track binning (again at the expense of downlinking fewer wavelengths due to bandwidth constraints). A future goal for the NP sensor is to provide 5 cross-track FOVs every 7.6 s at 50 km × 50 km resolution.

2. Sensor Performance

2.1. Signal-to-Noise

The use of empirical orthogonal function (EOF) decomposition analysis can help discern what patterns are present in the measurements and also to determine signal-to-noise ratio (SNR) values. If EOF analysis was used over the full wavelength interval, it would be dominated by viewing condition changes as well as ozone absorption that varies by an order of magnitude, and the normalization and polynomial fitting used to remove these broad-scale variations prior to the EOF analysis would not be able to handle the full spectral range well. Therefore, covariance matrices were constructed for each of the cross-track positions for three separate wavelength intervals (305–325, 320–345, and 340–380 nm) using six orbits of Earth view radiances. The regions were overlapped to test the consistency of the fits and analysis on the different wavelength intervals.

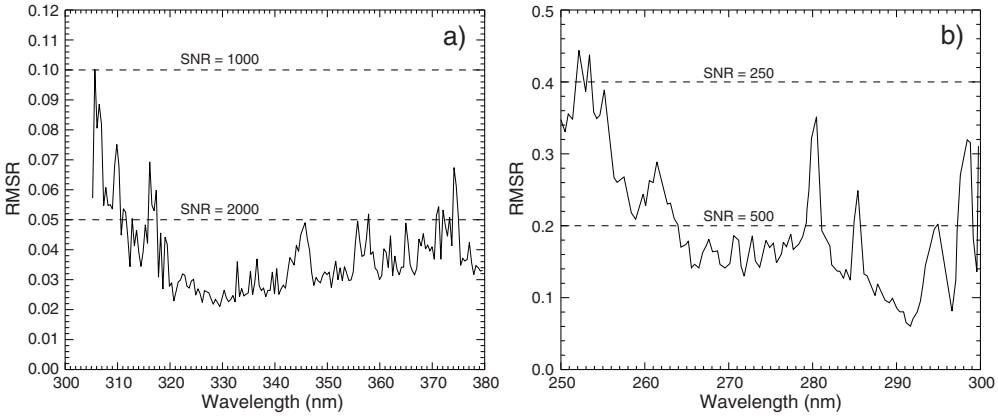

Figure 1. The root-mean-square residual (in percent) from an empirical orthogonal function analysis where the six largest patterns were removed with corresponding SNR values shown by the dotted lines. (a) For the NM sensor, the residuals equate to signal-to-noise ratios of better than 2000:1 for most wavelengths greater than 320 nm, dropping to 1000:1 at the shorter wavelengths. (b) For the NP sensor, the SNR varies from 550:1 at the longer wavelengths to 250:1 for the shortest; spikes correspond to lower signal levels due to solar lines at those wavelengths.

For a given across-track FOV, the radiances for each of the spectral intervals were normalized by using the overall average spectrum for the position and interval, as well as a third-degree polynomial fit in wavelength, before computation of the 105 covariance matrices (one for each of the 35 across-track positions for each of the three wavelength intervals). For each matrix, the total explained variance from the first six patterns was greater than 99% for the first two intervals and 95% for the third; any remaining patterns were 2 orders of magnitude smaller, have little to no influence on ozone retrievals, were regarded as noise, and were used to evaluate SNR.

Figure 1a shows the resulting root-mean-square residual values, in percent, for across-track FOV 11; these results are representative of those at other FOVs. They equate to an SNR of better than the 2000:1 at most wavelengths for most across-track FOVs, with the SNR dropping to 1000:1 only for the shortest wavelengths. Results from a similar analysis for the NP sensor, shown in Figure 1b, indicate SNRs from 500:1 at the longer wavelengths (with spikes for wavelengths at solar lines, where there is less signal), dropping to 250:1 at the shortest. The values for both the NM and NP sensors are either within or just above the specifications shown in Table 1.

2.2. Dark Current

Dark current resulting from electrons thermally excited into the CCD conduction band constitutes a systematic bias that must be removed from the OMPS sensor signals. Subtraction of dark current is a correction applied to all OMPS raw science data. Changes in pixel dark current rates are regularly measured for both the image and storage regions of the CCD during the dark part of the orbit. Dark current corrections for science data are constructed from measurements made once a week with the calibration mechanism in the closed position.

Dark current is well characterized and stable prior to launch, but it continuously evolves on orbit due to lattice damage caused by energetic solar wind or cosmic ray particles striking the CCD. Most changes are in the form of pixels developing permanently elevated dark current rates. Dark rates are a strong function of CCD temperature. Prelaunch rates are distributed normally, with means of approximately 2 counts per second (88 electrons) for the NM sensor (at -30C) and approximately 0.25 counts per second (11 electrons) for the NP sensor (at -45C); the standard deviations are close to 7%. Due to the accumulation of damaged pixels on orbit, the mean rates evolve approximately linearly at rates of 0.54 electrons per second per week for the NM sensor and 0.09 electrons per second per week for the NP sensor. However, individual damaged pixels may develop much higher rates, up to over 100 times the mean. A significant fraction of damaged pixels exceed the photon shot noise for typical Earth view signals, and even the nominal rates can exceed the noise level for weak signals.

While the effect of damaged pixels is captured by the dark correction, it is useful to characterize and track it in more than one way. In one approach, we apply a threshold of +8σ above the prelaunch dark current

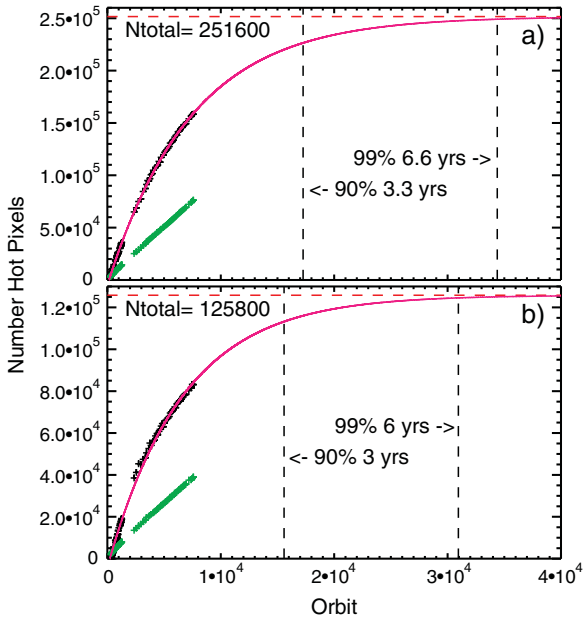

Figure 2. Nadir hot and damaged pixel evolution through April 2013 for the (a) NM and (b) NP sensors, as given by threshold detection and histogram-based counting methods. The number of damaged pixels counted by the histogram method (black points) is fitted by the expected exponential trend (purple). The threshold method to detect hot pixels (green points) underestimates the number of damaged pixels and gives a linear trend.

distribution mode; pixels that are identified form a subset of damaged pixels and are denoted as hot. We also track any pixels with elevated dark current due to damage, regardless of the level of increase. Identification of all damaged pixels is difficult, but a statistical method to count them has been developed. Histograms of dark current rates have evolved, with a change characterized by the reduction of the peak value and growth in the height of the upper wing, but with the mode unchanged from the prelaunch levels. Therefore, the undamaged fraction of pixels is represented by a Gaussian with the peak height of the histogram but the mode and standard deviation of the prelaunch distribution. The estimated number of damaged pixels is given by subtracting the area under this scaled prelaunch distribution from the total number of pixels. The number of pixels calculated in this way is more than twice the number given by the threshold method. Figure 2 shows the hot/damaged pixel number obtained both ways for the nadir sensors. Assuming that, statistically, pixels become damaged at a constant rate, the number of damaged pixels should be described by an exponential asymptotically approaching the total number of pixels. This function is a good fit to the calculated damaged pixel number. By extrapolating the fit, we predict that the fraction of damaged pixels will reach 90% in 3–3.3 years and 99% in 6–6.6 years from launch. The mean increase in dark current remains small compared to the total signal. For example, the change in the 265 nm signal amounts to approximately 0.25% over a period of 3 weeks.

A pixel is not considered hot enough to be unusable until it reaches a level too close to saturation to leave a sufficient dynamic range above it for normal photon signals. This defines a class of bad pixels that must be removed from use. Maximum dark current levels are currently about 250 counts for the NM sensor and 2500 counts for the NP sensor; maximum signal levels are about 12,000 and 8000 counts, respectively, and saturation is about 15,600 counts. For both OMPS sensors, this class of pixels is currently unpopulated. Another type of bad pixel is "cold," meaning completely unresponsive. These are tracked in the dark current through a lower threshold comparable to the upper threshold for hot pixels, and none have been detected.

Pixels can also exhibit random telegraph signal (RTS), which is another type of dark current change that can result from lattice damage [*Hopkins and Hopkinson*, 1993]. RTS pixels are hot pixels with two or more quasi-stable states. Transitions between levels occur at characteristic time scales that increase with decreasing CCD temperature. Studies indicate that RTS pixels in CCDs operating at the NM temperature, -35°C, will have stable periods approximately 40 times longer than a detector operating at -8°C. At NP temperatures, -45°C, the increase is nearly a factor of 800. Our preliminary analysis indicates that the majority of the OMPS RTS pixels have mean stable periods exceeding 1 week. This threshold is important because pixels with periods of less than 1 week are not corrected by the OMPS dark calibration updates. The effect of RTS pixels is also reduced when multiple pixels are combined into macropixels, as with OMPS. The behavior of RTS is complex, and their exact effect on the OMPS measurements is not completely understood at this time.

2.3. Linearity

OMPS calibration assumes a linear relationship between the incident photon energy and the analog to digital converter (ADC) output. The input/output chain consists of three steps: (1) conversion of photons to electrons

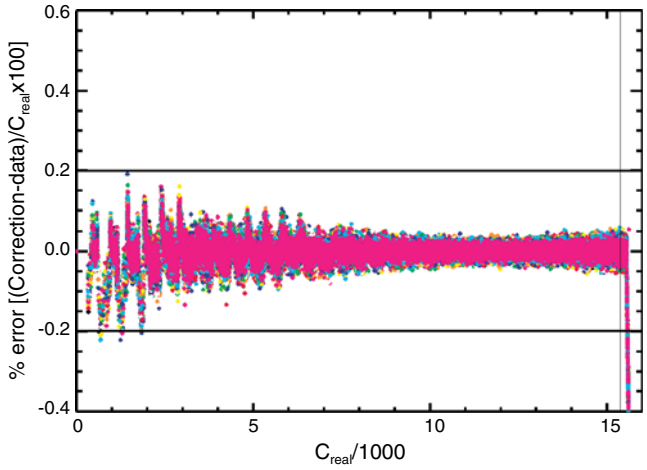

Figure 3. NP sensor linearity correction knowledge and stability. The ratio of the fit (correction) to the signal over ~1000 orbits. The system tolerance of 0.2% knowledge of nonlinearity is exceeded for virtually all individual points. The vertical line is the ADC saturation.

in the CCD pixel wells, (2) conversion of the charge readout of the CCD to voltages by an on-chip amplifier, and (3) conversion of the voltages to digital counts by the ADC. The method used to monitor signal linearity assumes that nonlinearities in photoelectron generation can be ignored when compared to the 0.2% linearity knowledge requirement. The observed 2% nonlinearity is primarily caused by the on-chip amplifier.

Linearity measurements consist of aperture door-closed data taken weekly, with onboard light-emitting diodes (LEDs) illuminating the CCDs in a series of exposure times in 60 ms steps from 0 to 2.4 s. Time linearity of the photoelectron generation is assumed, provided that the LED output is constant. Slight LED drift does occur over the course of the stepped sequence, which is compensated for by interleaving 500 ms reference frames with the stepped exposures. These reference measurements are used to adjust the effective exposure time for each time interval.

Linearity is defined relative to the measured signals at two points. The lower limit was set at the bias level; the upper limit was set prelaunch to be 75% of the ADC saturation point. Individual pixel responses are converted from actual counts (C_{real}) to ideal counts (C_{ideal}) by scaling with the adjusted exposure times by the slope between the two points, and the linearity correction is then determined by fitting a fifth-degree polynomial to the difference $C_{ideal} - C_{real}$. Plots of the fit (correction) minus the fit data divided by the signal for all points over an ~1000 orbit range are shown in Figure 3 for the NP sensor; these results are also representative of those for the NM sensor. The difference between the fit and the data demonstrates that the 0.2% prelaunch knowledge specification over the full dynamic range is met. Since points for all orbits essentially overlay each other, the plots also show that the linearity corrections are stable; the change over 1000 orbits is no greater than 0.01%. Pixels that never reach the upper tie point in the stepped exposure sequence define a class of bad LED pixels that are excluded from the fit. These few cold spots in the LED response are thought to be caused by dust or other contaminants on the LED itself.

2.4. Transients

During the early orbit, "doors-closed" checkout phase of the mission, the OMPS sensors obtained special dark measurements designed to characterize the orbital energetic particle environment. Of particular interest are transient signals from the particle flux in the South Atlantic anomaly (SAA) [*Hajdas et al*., 2003] and their impact on the OMPS signals.

The OMPS NM and NP sensors took transient monitoring data between November 2011 and January 2012. Images were collected at 3–4 times the nominal Earth view temporal resolution on the day and night sides of 156 orbits. Transient events were isolated by using an approach where the time series is median filtered, pixel-by-pixel, and values greater than a threshold over the median are flagged as transients. An image of dark rates is then calculated from the mean of the nontransient values for each pixel. Finally, time-resolved images were produced by transient signal distributions on the CCD focal plane, and statistics on transient energy and number density were compiled.

The impact of SAA transients on nadir sensor Earth view signals is illustrated by histograms of measured transient energies shown in Figure 4. The histograms represent transient energies (expressed in counts) recorded by the NM (Figure 4a) and NP (Figure 4b) sensors during hypothetical Earth view exposures at the peak of the SAA. Mean rates are 4.2 (NM) and 48.3 (NP) transients per Earth macropixel measurement.

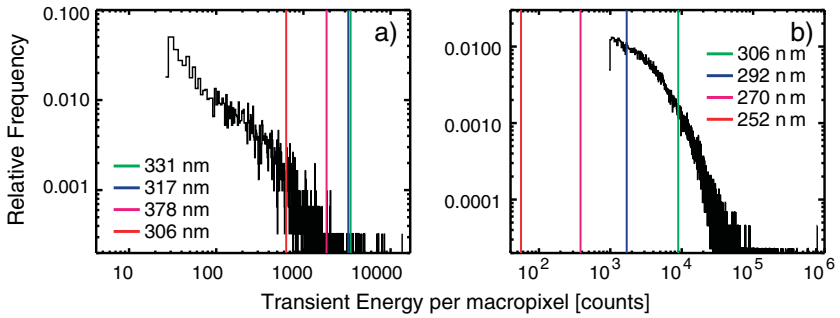

Figure 4. The impact of SAA transients on nadir sensor Earth view signals for (a) NM sensor and (b) NP sensor. Different vertical lines represent thresholds of 1% of the signal for four wavelengths for each sensor. The integral of the curve above the thresholds is the fraction of macropixels impacted at greater than 1% of the signal: 0.59% 331 nm, 0.62% 317 nm, 1.8% 378 nm, and 15% 306 nm (NM); 18.6% 306 nm, 83% 292 nm, 100% 270 nm and 252 nm (NP).

Thresholds overplotted in Figure 4 represent 1% of the measured Earth radiances (expressed in counts) at four wavelengths for each sensor. Reference signals are averages of all cloud-free radiances taken near the vernal equinox within the latitude limits of the transient data but outside of the SAA longitudes.

The fraction of transients exceeding 1% radiance (area of histogram above thresholds) was calculated. The results are summarized in Tables 2 and 3. For the four wavelengths on the NM sensor, the largest number of macropixels above the 1% threshold (15%) occurred at 306 nm, while the minimum number (0.59%) occurred at 331 nm. For the NP sensor, 100% of the macropixels were found to be above the 1% threshold at 252 and 270 nm, while the minimum number (18.69%) occurred at 306 nm. The mean radiance error due to transients was also calculated for each wavelength/sensor. The minimum mean error for the NM sensor is 0.10% at 331 nm, with a maximum of 0.55% at 306 nm. While the minimum mean error for the NP sensor is 0.72% at 306 nm, the maximum is 115% at 252 nm. Because the errors are so large for the shorter wavelengths, the NP measurements are currently unreliable inside the SAA. However, since the ozone profile retrievals from the NP sensor are only used to provide a link to historical data sets of ozone profile and to provide a way to directly evaluate ozone profile retrievals from the OMPS LP sensor, they are not needed to satisfy the top-level requirements for the JPSS system. We are investigating methods for flagging transients in macropixels, which will likely be most effective at the shortest NM wavelengths.

Spatial distributions of transient number density (pixel^{-1} s^{-1}) and mean energy per transient (counts) measured by the two sensors are similar to those for the limb sensor and are discussed in the companion limb calibration paper. Observed transient number densities in both the north and south polar auroral regions are less than 2.5% of the peak density in the SAA.

3. Calibration

The retrieval algorithms designed to work with the OMPS nadir sensors utilize a normalized radiance (NR), which is the ratio of measured Earth radiance to measured solar irradiance [*Bhartia et al.*, 2013; *Rodriguez et al.*, 2003]. Radiometric requirements that allow OMPS to meet its ozone accuracy and precision specifications are based on NR also referred to as top-of-the-atmosphere reflectance. The solar irradiance is measured by rotating a solar illuminated aluminum diffuser into a position in front of the sensor field-of-view to produce a diffuse radiance. Since the solar diffuser precedes the same optics used in Earth radiance measurements, many systematic errors are cancelled in the NR, and the sensitivity to calibration errors, such as optical throughput and electronic gain, is significantly reduced (but not eliminated). As a consequence, the uncertainties in radiance and irradiance calibrations are allowed to be quite large (8% and 7%, respectively), while the uncertainty in the NR is required to be less than 2%.

Table 2. OMPS NM SAA Transient Signals Compared With the Vernal Equinox Cloud-Free Radiances

Wavelength (nm)	Radiance (counts)	Macropixel (%) >1% rad	Mean Error (% rad)
331	348,158	0.59	0.10
317	327,406	0.62	0.11
378	184,325	1.8	0.19
306	63,494	15	0.55

Table 3. OMPS NP SAA Transient Signals Compared With the Vernal Equinox Cloud-Free Radiances

Wavelength (nm)	Radiance (counts)	Macropixel (%) >1% rad	Mean Error (% rad)
306	893,969	18.6	0.72
292	169,558	83	3.8
270	38,240	100	17
252	5,614	100	115

Following the successful approach of heritage instruments [*Jaross et al*., 1995], working and reference diffusers are used to monitor long-term diffuser change. To measure over the full 110° of the OMPS telescope, the diffuser is rotated to a series of seven positions; each position overlaps with the position before and after it, and measurements from the seven positions are "stitched" into a single plane of solar irradiance. A separate measurement at the nadir position is also collected for the NP sensor. The working diffuser is deployed every 2 weeks, while the reference diffuser is used once every 6 months, thus limiting the effects of contamination. Whenever a diffuser is not in use, it is protected from exposure to UV radiation and contamination by the calibration housing.

3.1. Diffuser Features

The use of diffusers in optical instrumentation results in interference patterns in the reflected signal due to localized coherency. The effect is exacerbated with front-surface aluminum diffusers, where most photons are reflected only once, and when array detectors are used [*van Brug et al*., 2004]. In the case of the OMPS nadir sensors, the resulting interference patterns have spectral periodicity of 10 nm to 20 nm and across-track spatial periods of approximately 10°. Peak-to-peak variations are as much as 10% but smaller when adjacent pixels are combined into macropixels.

The patterns, referred to as diffuser features, are very sensitive to the angle of illumination. Consequently, solar measurements collected over the course of a year by each pixel vary with apparent randomness by as much as 10%. These variations are not actually random and are quite repeatable when incidence angles are the same. During the prelaunch irradiance calibration of OMPS, this angle-dependent response was measured, and the resulting corrections have been incorporated into solar data processing. Since the prelaunch characterization was very time consuming, the angular step size used was no smaller than needed to meet the calibration requirements.

Figure 5a illustrates these features by showing the ratio of two solar flux measurements taken 1 month apart using the nadir position of the diffuser. These measurements were collected in a sequence where the diffuser is deployed to all seven positions over a period of 5 min. Since the change in solar angle is less than 1° within each of the seven data sets, little natural smoothing of the features occurs, and the pixel-to-pixel variation in this case approaches 5%.

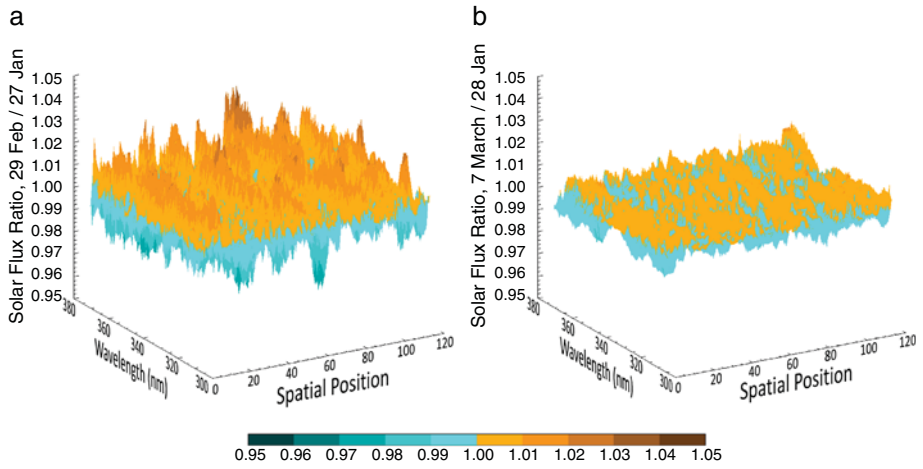

Figure 5. Ratios of solar flux measurements taken with: (a) the nominal solar calibration sequence using 3 exposures for each measurement; and (b) a sequence using 23 exposures for each measurement. The effects of diffuser interference features are greatly reduced in the modified sequence, which has subsequently been adopted for use.

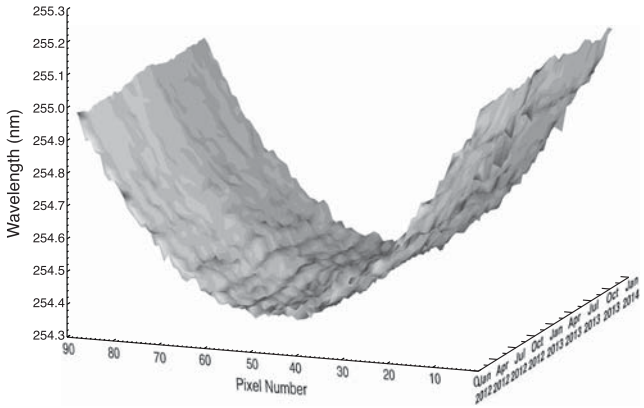

Figure 6. Surface plot showing the results of wavelength registration for one of the NP sensor wavelengths. The 0.7 nm spectral smile is clearly seen. Smaller scale features are also noticeable. The structure of these features indicates that they are not noise but due to a combination of sensor effects, including slit irregularities and seasonal wavelength shifts.

To mitigate the effect of these features, a different calibration sequence was subsequently implemented for all solar flux measurements. In the new sequence, the incidence angle can vary by as much as 6° for each position. The corresponding change in diffuser features significantly dampens the variations between pixels. Figure 5b exhibits variations of no more than 1% for a similar 1 month separation in solar measurements. The semiannual solar measurements using the reference diffuser are scheduled to always occur at the same solar incidence angle, thus reducing the uncertainty in the long-term calibration drift caused by the diffuser features.

We note that, although the new calibration sequence serves to reduce the effect of these features, the results shown in Figure 5b indicate that they are not completely eliminated; while the current magnitude of these features does not adversely affect ozone retrievals, they are of concern for retrievals that are more sensitive to small calibration effects such as SO_2 [*Yang et al*., 2013]. Methods and techniques to further reduce the effect are actively being investigated. We also note that the next flight model of OMPS may employ volume diffusers, for which diffuser features are significantly reduced.

3.2. Wavelength Calibration

Wavelength calibration is also performed with the solar flux measurements by making use of the spectral structure of the solar Fraunhofer lines. A Levenberg-Marquardt nonlinear least squares algorithm is implemented to optimize the set of spectral band centers for each fitting window. Band centers are represented by a polynomial function of the spectral indices for each spatial position. A high-resolution (0.01 nm sampling) solar reference flux [*Dobber et al*., 2008], slightly shaped by a parabolic function of the spectral index, is then convolved at the band centers using preflight bandpasses (slit functions) to form a synthetic spectrum. The resulting spectrum is compared with the measured irradiance. Band centers are varied to minimize the difference between the synthetic and measured spectra. The sensors measure unique spectra at each spatial position, and the regression is performed on each separately. The output of the process is a set of band center wavelengths for every macropixel measured by the sensor.

The results from applying the above algorithm to the first year and a half of solar measurements taken by the NP sensor are shown in Figure 6 for one wavelength. First, the approximately 0.7 nm spectral distortion across the CCD is clearly evident. Second, small-scale structure can be seen both across the CCD and in time. Regression with a smooth polynomial in either the spectral or spatial dimension yields a residual variation of 0.01 nm. A close examination of this structure in Figure 6, however, indicates that it is not random in nature and therefore not simply noise; preliminary investigations indicate that it is due to a combination of factors, including slit irregularity effects and seasonally dependent wavelength shifts. This analysis indicates that the accuracy of the OMPS wavelength registration is at least 0.01 nm and likely better.

To investigate wavelength registration differences between solar and Earth view measurements from the NM sensor, the algorithm described above can be adapted to use Earth view data for wavelengths with no ozone absorption (those greater than 340 nm). As seen in Figure 7, application of the algorithm to measurements along the orbit indicate a clear intraorbital shift between solar and Earth view measurements of 0.03 nm; this is the result of thermal changes on the sensor. Because of ozone absorption, the wavelength regression cannot easily be adapted for use with the NP sensor. However, the application of other techniques, including multivariable fits to the data (see section 3.4), indicates minimal intraorbital shifts of the NP Earth view wavelength scale from the solar one.

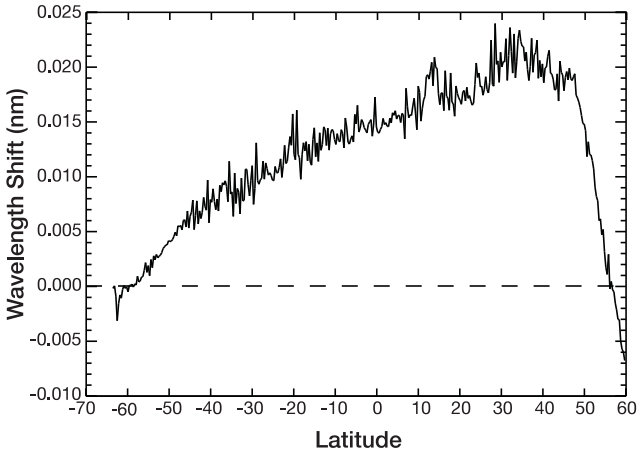

Figure 7. The difference between wavelength registration spectra for Earth view and solar measurements. The intraorbital shift dependence is related to thermal changes at the sensor. The Earth view data were taken on 7 December 2012.

3.3. Normalized Radiance Calibration

Comparisons with data from the well-calibrated [*Jiang et al*., 2007; *Schwartz et al*., 2008] Microwave Limb Sounder (MLS) sensor flying on Aura have been used in order to evaluate the performance of the NRs that are the central component of the retrieval algorithms. The MLS measurements made during June 2012 were colocated, within 50 km, with measurements from the OMPS sensors; MLS profiles of ozone and temperature were then input, along with the viewing conditions of the OMPS sensors, to a radiative transfer code to calculate the corresponding NRs. For comparison purposes, the temperature profile from the MLS was assumed to be accurate along the entire altitude (pressure) range. For ozone, the MLS profile was assumed to be accurate down to 250 hPa; below 250 hPa, the MLS profile was replaced by one from the Logan, McPeters, and Labow climatology [*McPeters et al*., 2007] corresponding to the latitude and time of the MLS measurement. To eliminate cloud effects, the reflectivity determined by the OMPS sensors was used to constrain the matchup data set to one where the reflectivity was less than 0.10; to minimize absorbing aerosol effects, the aerosol index determined by OMPS was constrained to be no larger than 1.0 (see *Flynn*, *et al*. [this issue] for details on the reflectivity and aerosol index determinations). To further constrain the matchup data set, only colocated data between 20 degrees south and 20 degrees north latitude were used. The NRs thus calculated represent what OMPS should have measured, assuming that the MLS profiles are accurate. These calculated values were then compared with the NRs actually measured by the OMPS NM and NP sensors.

3.3.1. OMPS NM Sensor

Figure 8a shows the comparison of measured NRs for the most nadir-looking across-track FOV (number 19) to calculated NRs averaged for all colocated matchups. A large deviation between the calculated and measured NRs is seen shortward of 310 nm, increasing with decreasing wavelength. While the system specification

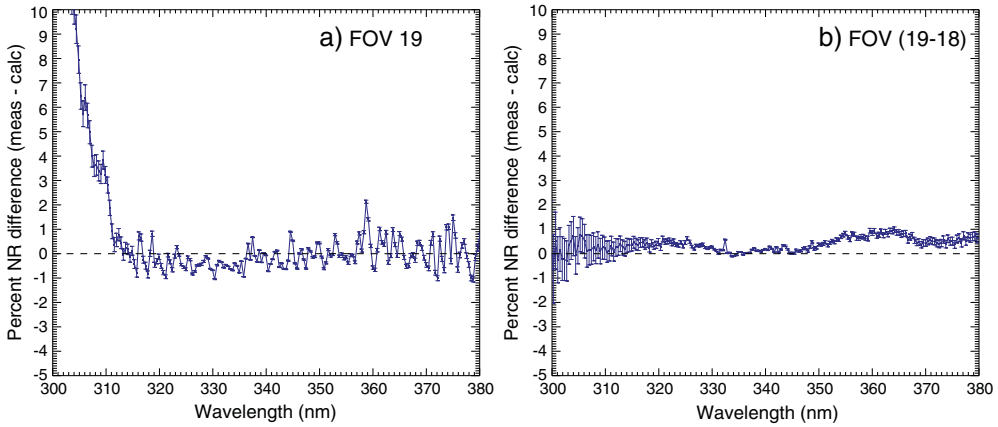

Figure 8. (a) A comparison of NRs calculated using MLS ozone and temperature profiles colocated with OMPS retrievals using the OMPS viewing conditions for cross-track position 19. The average is over 20°S to 20°N latitude for June. (b) A comparison of NRs where the difference for position 18 is subtracted from position 19. The error bars represent the standard deviation of the mean.

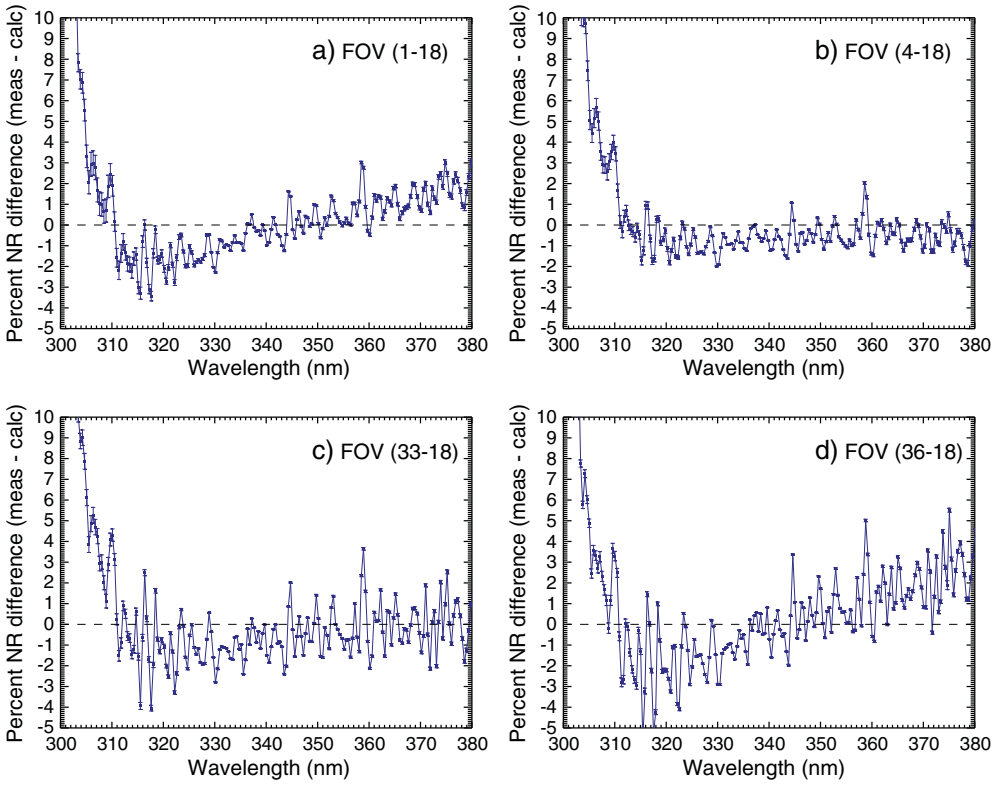

Figure 9. Similar comparison to Figure 8 for different cross-track positions. Although the difference for cross-track position 18 is subtracted, structure is still seen in the far off-nadir positions because physical effects such as Raman scattering and wavelength registration effects are different than those at position 18 and are therefore not fully accounted for. The error bars represent the standard deviation of the mean.

requirement for the sensor was for stray light errors to be no larger than 2%, prelaunch measurements indicated that the sensor did not meet this requirement below 310 nm, with the magnitude of the stray light increasing with decreasing wavelength. Most of the NR error seen in Figure 8a results from uncorrected stray light, although some of it also results from temperature dependence in the radiometric sensitivity. Neither effect is corrected for in this figure, although future plans include corrections for them. Since the algorithm designed for use with the NM sensor uses only one wavelength shorter than 310 nm (at 308 nm) and can be modified not to use any, the fact that the sensor falls outside the stray light specification at these wavelengths has little impact on ozone retrieval.

Because the overall agreement between the calculated and measured NRs above 310 nm is within the 2% system specification for NR, stray light effects at these wavelengths are also within their 2% specification. The peak-to-peak variation of about 2% is either caused by physical effects not included in the radiative transfer code, such as Raman scattering, or sensor effects, such as wavelength registration errors. This is demonstrated in Figure 8b, where the percent difference between measured and calculated NR at FOV 18 is subtracted from the percent difference between measured and calculated NR at FOV 19; this virtually eliminates the peak-to-peak variation and brings the agreement between measured and calculated NRs to well within 1%.

The behavior of the NM sensor for the far off-nadir FOVs is shown in Figure 9. The comparisons indicate that, while the sensor is within its specification out to FOVs 4 and 33, significant differences begin to emerge at the very outermost FOVs (1 to 3 and 34 to 36). First, although the difference for cross-track FOV 18 is subtracted, structure is still seen in the far off-nadir FOVs because physical effects such as Raman scattering and sensor effects such as wavelength registration are different than those at FOV 18 and are therefore not fully accounted for. Second, a roughly linear dependence with wavelength can be seen. It should be noted that similar problems with retrievals at far off-nadir FOVs have been seen in the heritage sensors as well.

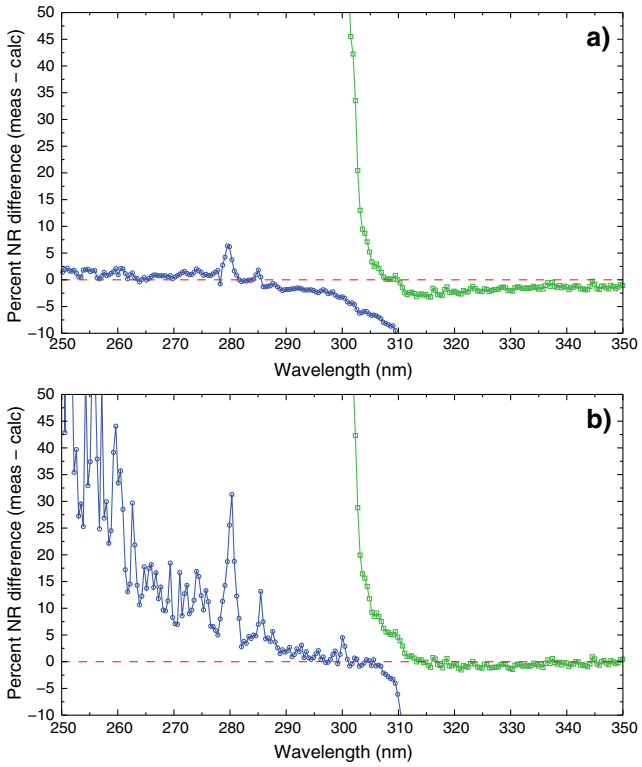

Figure 10. Comparison of measured OMPS NRs with NRs calculated using colocated MLS profiles for: (a) a matchup located outside the region of the SAA; and (b) a matchup located inside the SAA; and The effect of the SAA is significant for wavelengths less than 290 nm.

Differences at these FOVs can be due to a number of reasons, possibly including a problem with representing the larger far off-nadir FOV in the radiative transfer calculations. Since, unlike with the heritage sensors, the OMPS FOV can be varied, we plan to use this feature to further study far off-nadir issues affecting both these systems and heritage systems.

3.3.2. OMPS NP Sensor

Because of the large FOV (250 km × 250 km) for the NP measurement, the radiative transfer code was run 30 separate times using the viewing conditions of the 30 colocated (6 across-track by 5 along-track) FOVs of the NM sensor and then averaged together. Shown in blue in Figure 10 are two examples of results from individual matchups of MLS with OMPS; Figure 10a shows a comparison outside the SAA, while Figure 10b shows a comparison inside the SAA. The transient effect on the NP measurements described earlier can clearly be seen for all wavelengths less than 290 nm.

For the current study, all comparisons inside the SAA have been excluded, and Figure 11 shows the results after averaging over all the remaining colocated matchups. Although the overall difference between measured and calculated NR values clearly increases from longer to shorter wavelengths, the comparison indicates that, except for spikes seen at the locations of the Mg II absorption lines at 280 and 285 nm, the measurements satisfy the NR and stray light specifications shown in Table 1. The spikes can be attributed to stray light since, at these wavelengths, the signal level is lower than the signal level of the surrounding wavelengths.

Also shown (in green) in Figure 11 is the comparison of the averaged 30 NRs from the NM sensor to NRs calculated for each of the 30 NM FOVs, both in the overlap region and for longer wavelengths. A discrepancy is seen when these results are compared to the results shown in Figure 8. This discrepancy is due to the fact that the comparison shown in Figure 11 uses an average of measured NRs from the 30 NM FOVs that correspond to the much larger NP FOV; larger variations in the scene characteristics for the larger FOV cause larger differences between the calculation using the colocated MLS profiles and the averaged OMPS measurements. This is particularly important for wavelengths longer than 300 nm, where surface effects become significant.

Also of interest is the overlap region between the NP and NM sensors. As stated earlier, not all of the sharp increase seen in the NM sensor from 310 to 300 nm is due to stray light; furthermore, the corresponding drop in the NP sensor seen from 300 to 310 nm cannot be attributed to stray light at all. The NM and NP sensor responses change rapidly in this spectral range due to the dichroic filter. There are two effects that contribute to radiometric errors: changes in wavelength registration relative to ground calibrations and changes in the filter's reflectivity. Both have their origins in the nearly 25°C change in optical bench temperature between ground measurements and orbit. The observed band center wavelength change is approximately 0.1 nm in the NM sensor. Preliminary studies indicate that a 0.15–0.25 nm shift in the dichroic transmission function would, at least to first order, eliminate the discrepancy. Work is currently under way to further characterize and understand such dichroic effects.

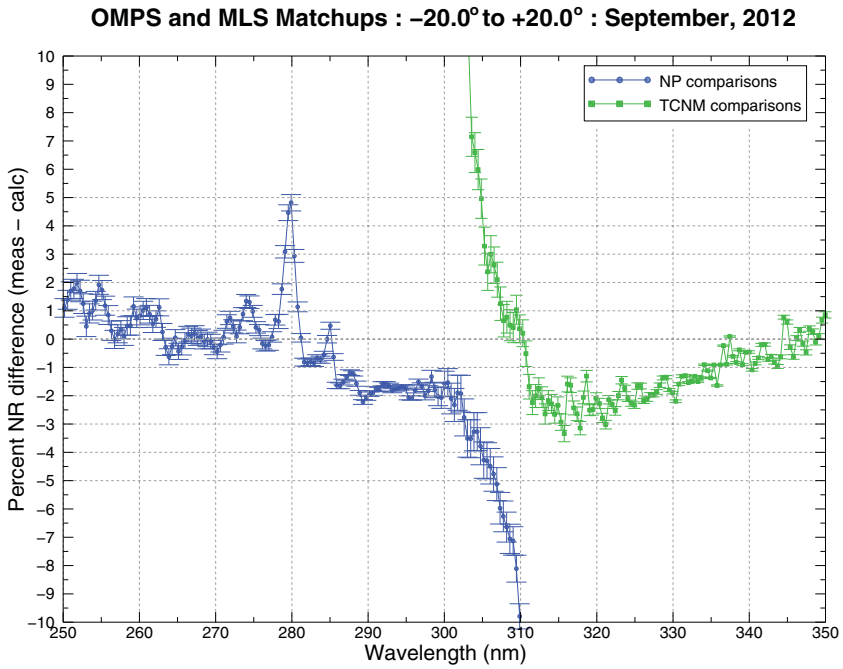

Figure 11. Comparison of NRs calculated using MLS profiles colocated with measurements from the NP sensor (scale has been reduced from Figure 10). The NP measurements currently consist of only one 250 km × 250 km FOV; the viewing conditions for each of the 30 colocated NM FOVs (6 across track by 5 along track) are used in the calculation. The results show the mean difference for all of the MLS-NP matchups in June between 20°S and 20°N latitude outside of the SAA region. The error bars represent the standard deviation of the mean.

3.4. Stability

In order to provide data that can contribute to a long-term data record, the OMPS sensors must be stable or, if a drift is identified, the drift must be correctable. Figure 12a shows the time dependence of solar flux measurements taken from the central part of the diffuser over the first year and a half of the mission for one of the NM sensor wavelengths (317 nm); these measurements are representative of those at other wavelengths and diffuser positions. The results represent all of the measurements from the working diffuser, along with those from the four reference diffuser measurements that have been performed. Figure 12a indicates that there is no degradation in either the working or reference diffuser measurements.

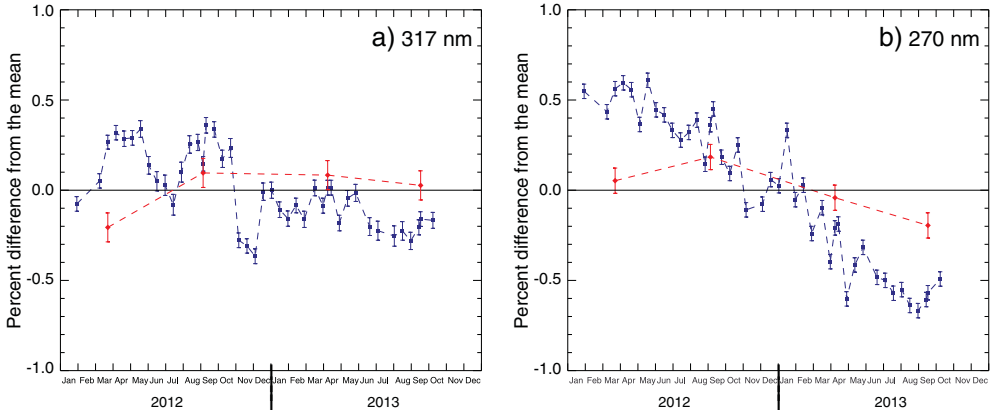

Figure 12. Time dependence of the solar flux measurements from the central part of the diffuser for (a) the 317 nm wavelength on the NM sensor and (b) the 270 nm wavelength on the NP sensor. Blue represents the working diffuser measurements, while red represents the reference diffuser measurements. No degradation is seen for the NM sensor. For the NP sensor, comparison of measurements between the working (green) and reference (red) diffusers indicate that half the 1% degradation seen is most likely due to diffuser degradation. The error bars represent the standard deviation of the mean.

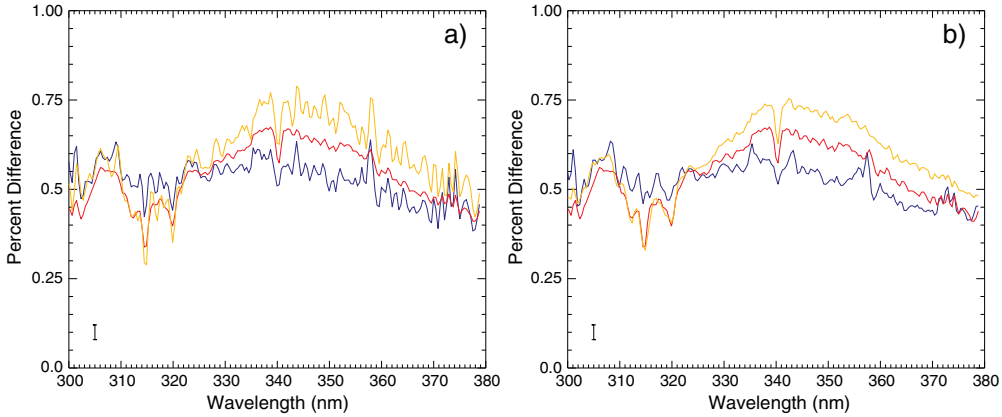

Figure 13. (a) The percent difference between the NM solar flux measurements from the reference diffuser for 31 August 2012 (blue line), 4 April 2013 (red line), and 28 August 2013 (gold line) and the solar flux measurements from the reference diffuser for 21 March 2012. (b) The wavelengths have been shifted by 0.002 nm for 31 August 2012 and 28 August 2013 with respect to the results in Figure 13a. The error bar shown on each plot represents the standard error of the mean for each wavelength.

The time dependence for the NP sensor, shown in Figure 12b, indicates 1% degradation for the NP sensor's working diffuser measurements over the first year and less than 0.5% degradation for the four reference diffuser measurements over the same time period. Given the assumption that the reference diffuser has not degraded, these measurements suggest that half the change occurs in the working diffuser and half is in the remainder of the sensor.

Comparisons between solar flux measurements taken over time can also be used to determine if any seasonal wavelength shift is taking place in the NM sensor. The reference diffuser measurements are used for this study because measurements from the reference diffuser are taken during times where the solar incidence angle is the same; this minimizes both goniometric differences and diffuser effects. For each reference measurement, the solar flux values from all of the exposures for all seven diffuser positions are used; all of the spatial rows illuminated for each exposure at each diffuser position are interpolated to a common wavelength scale and then averaged to provide one solar flux measurement for each wavelength.

In Figure 13a, the ratios of the reference diffuser measurements taken on 28 August 2012, 4 April 2013, and 31 August 2013 to those taken on 21 March 2012 are shown. In this figure, an overall offset of approximately 0.5% is seen between the last three reference measurements and the first measurement; the cause of this discrepancy is still being investigated. One can also see in this figure that the consistency between the first and third reference measurements (taken 12 months apart) is better than the consistency between the first and the other measurements (taken 6 and 18 months after the first). Figure 13b shows that a 0.002 nm shift applied to the August measurements produces a marked improvement in consistency, indicating only a minimal seasonal dependence in the NM sensor's wavelength calibration.

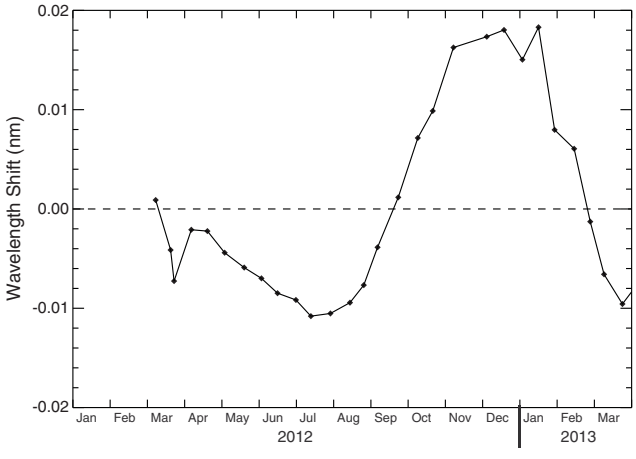

Figure 14. Seasonal wavelength shift determined by a multivariable fit to the NP sensor solar data.

For wavelengths less than 290 nm, changes in solar activity complicate the use of solar measurements over time to determine seasonal wavelength shifts. A more detailed multivariable regression was therefore undertaken to determine any such shift. First, the values were averaged over the spatial dimension of the CCD array (93 pixels) for each measurement at each wavelength. Then, the regression model

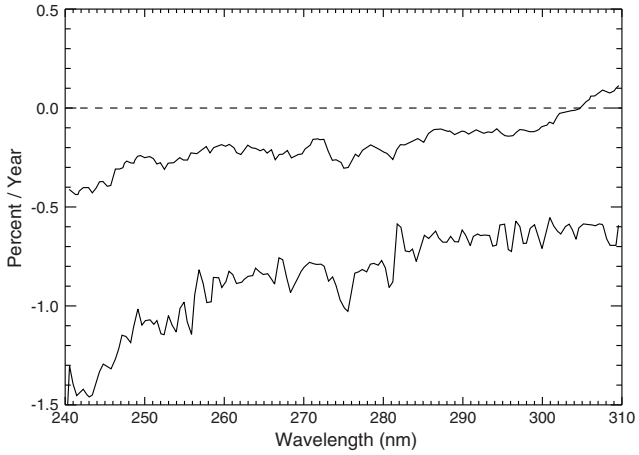

Figure 15. Trend terms from the multiple linear regression model. The upper line is the reference diffuser trend term and the lower line is the working diffuser trend term. If we assume that the reference diffuser is stable, then the pattern in the reference diffuser term represents sensor throughput changes.

was applied to the data using three different trend terms: one representing solar activity using the Mg II core-to-wing ratio as a proxy [*DeLand and Cebula*, 1993], one representing a wavelength scale shift, and one representing sensor plus diffuser change.

Results for the wavelength shift term, shown in Figure 14, indicate a seasonal wavelength shift of 0.03 nm. This temporal pattern is found to track the optical bench temperature's seasonal variations well. The results for the term representing sensor response change, converted to percent per year, are displayed in Figure 15. The upper line is the reference diffuser measurement trend term, and the lower line is the working diffuser trend term. Again, if we assume that the reference diffuser is stable, then the pattern in the reference diffuser term represents sensor throughput changes. These results, which indicate a sensor degradation of 0.5% per year at the shortest wavelengths, decreasing to no degradation for the longest wavelengths, are consistent the analysis shown in Figure 12b.

4. Summary

Extensive postlaunch analysis of data from the OMPS nadir sensors indicates that both the NM and NP sensors are generally performing within their prelaunch specifications. Analysis of dark current for both sensors (as well as the limb sensor) indicates that it is well understood and that the current procedure of updating it weekly is sufficient; we will continue to monitor it and, if it becomes necessary, the frequency of updates will be increased. Calibration issues concerning diffuser features have been mitigated through modification to prelaunch calibrations procedures; such features have now been reduced to less than 1%. Although stray light has been shown to be generally within the prelaunch specification of 2% for both sensors, issues at the shortest wavelengths (for the NM sensor) and the longest wavelengths (NP sensor) have been identified and will be corrected for in the future. Furthermore, issues concerning the dichroic filter that affect measurements from both sensors between 300 and 310 nm have been discovered, and a correction is being developed. Finally, analysis of solar flux measurements from the first year and a half indicate that both sensors are stable and that any degradation can easily be identified and corrected.

Acknowledgments

All of the data used in this paper are available through NASA's Ozone Product Evaluation and Test Element (PEATE) web site at http://ozoneaq.gsfc.nasa.gov/omps. The authors gratefully acknowledge the assistance of the PEATE team in processing the data used in this evaluation. We also thank the reviewers for their detailed comments and suggestions, which served to substantially improve the value of this paper.

References

Bhartia, P. K., R. D. McPeters, L. E. Flynn, S. Taylor, N. A. Kramarova, S. Frith, B. Fisher, and M. DeLand (2013), Solar Backscatter UV (SBUV) total ozone and profile algorithm, *Atmos. Meas. Tech.*, *6*, 2533–2548, doi:10.5194/amt-6-2533-2013.

DeLand, M. T., and R. P. Cebula (1993), Composite Mg II solar activity index for solar cycles 21 and 22, *J. Geophys. Res.*, *98*(D7), 12,809–12,823, doi:10.1029/93JD00421.

DeLand, M. T., S. L. Taylor, L. K. Huang, and B. L. Fisher (2012), Calibration of the SBUV version 8.6 ozone data product, *Atmos. Meas. Tech. Discuss.*, *5*, 5151–5203, doi:10.5194/amtd-5-5151-2012.

Dittman, M. G., E. Ramberg, M. Chrisp, J. V. Rodriguez, A. L. Sparks, N. H. Zaun, P. Hendershot, T. Dixon, R. H. Philbrick, and D. Wasinger (2002), Nadir ultraviolet imaging spectrometer for the NPOESS Ozone Mapping and Profiler Suite (OMPS), Proc. SPIE 4814, Earth Observing Systems VII, 111, September 25, doi:10.1117/12.453748.

Dobber, M., R. Voors, R. Dirksen, Q. Kleipool, and P. Levelt (2008), The high-resolution solar reference spectrum between 250 and 550 nm and its application to measurements with the Ozone Monitoring Instrument, *Sol. Phys.*, *249*, 281–291, doi:10.1007/s11207-008-9187-7.

Hajdas, W., C. Eggel, C. Wigger, D. Smith, H. Sanctuary, and A. Zehnder (2003), Spacecraft activation and south atlantic anomaly profiles measured with the RHESSI satellite, in *Proceedings of the 7th European Conference on Radiation and Its Effects on Components and Systems, RADECS 2003*, pp. 607–610, ESA, Noordwijk.

Hopkins, I. H., and G. R. Hopkinson (1993), Random telegraph signals from proton-irradiated CCDs, *IEEE Trans. Nucl. Sci.*, *40*(6), 1567–1574, doi:10.1109/23.273552.

Jaross, G., A. Krueger, R. P. Cebula, C. Seftor, U. Hartmann, R. Haring, and D. Burchfield (1995), Calibration and post-launch performance of the Meteor-3/TOMS instrument, *J. Geophys. Res.*, *100*(D2), 2985–2995, doi:10.1029/94JD02317.

Jiang, Y. B., et al. (2007), Validation of the aura microwave limb sounder ozone by ozonesonde and lidar measurements, *J. Geophys. Res.*, *112*, D24S34, doi:10.1029/2007JD008776.

McClain, S. C., P. W. Maymon, and R. A. Chipman (1992), Design and analysis of a depolarizer for the NASA Moderate Resolution Imaging Spectrometer – Tilt (MODIS-T), *Proc. SPIE*, *1746*, 375–385, doi:10.1117/12.138811.

McPeters, R. D., G. J. Labow, and J. A. Logan (2007), Ozone climatological profiles for satellite retrieval algorithms, *J. Geophys. Res.*, *112*, D05308, doi:10.1029/2005JD006823.

Rodriguez, J. V., C. J. Seftor, C. G. Wellemeyer, and K. Chance (2003), An overview of the nadir sensor and algorithms for the NPOESS ozone mapping and profiler suite (OMPS), *Proc. SPIE*, *4891*, doi:10.1117/12.467525.

Schwartz, M. J., et al. (2008), Validation of the aura microwave limb sounder temperature and geopotential height measurements, *J. Geophys. Res.*, *113*, D15S11, doi:10.1029/2007JD008783.

Seftor, C. J., J. C. Larsen, T. J. Swissler, J. V. Rodriguez, Q. Remund, G. Jaross, and C. G. Wellemeyer (2003), OMPS total column algorithm performance: Comparison to TOMS and to NPOESS Requirements, *Proc. SPIE*, *4891*, doi:10.1117/12.466109.

Stolarski, R. S., and S. M. Frith (2006), Search for evidence of trend slow-down in the long-term TOMS/SBUV total ozone data record: The importance of instrument drift uncertainty, *Atmos. Chem. Phys.*, *6*, 4057–4065, doi:10.5194/acp-6-4057-2006.

van Brug, H., R. Vink, J. Groote Schaarsberg, G. Bazalgette Courreges-Lacost, and B. Snijders (2004), Speckles and their effects on spectrometers due to on-board diffusers, *Proc. SPIE 5542*, Earth Observing Systems IX, pp. 334–341, doi:10.1117/12.559596.

Yang, K., R. R. Dickerson, S. A. Carn, C. Ge, and J. Wang (2013), First observations of SO_2 from the satellite Suomi NPP OMPS: Widespread air pollution events over China, *Geophys. Res. Lett.*, *40*, 4957–4962, doi:10.1002/grl.50952.